

1  
2  
3  
4  
5  
6  
7  
8  
9  
10  
11  
12  
13  
14  
15  
16  
17  
18  
19  
20  
21  
22  
23  
24  
25  
26  
27  
28  
29

**Improvements to the OMI near UV aerosol algorithm using A-train CALIOP and  
AIRS observations**

**O. Torres, C. Ahn and Z. Chen**

**(Submitted to AMT, May 1013)**

30 **Abstract.**

31 The height of desert dust and carbonaceous aerosols layers and, to a lesser extent,  
32 the difficulty in determining the predominant size mode of these absorbing aerosol types,  
33 are sources of uncertainty in the retrieval of aerosol properties from near UV satellite  
34 observations. The availability of independent, near-simultaneous measurements of  
35 aerosol layer height, and aerosol-type related parameters derived from observations by  
36 other A-train sensors, makes possible the use of this information as input to the OMI  
37 (Ozone Monitoring Instrument ) near UV aerosol retrieval algorithm (OMAERUV). A  
38 monthly climatology of aerosol layer height derived from observations by the CALIOP  
39 (Cloud-Aerosol Lidar with Orthogonal Polarization) sensor, and real-time AIRS  
40 (Atmospheric Infrared Sounder) CO observations are used in an upgraded version of the  
41 OMAERUV algorithm. AIRS CO measurements are used as a reliable tracer of  
42 carbonaceous aerosols, which allows the identification of smoke layers in regions and  
43 seasons when the dust-smoke differentiation is difficult in the near-UV. The use of CO  
44 measurements also enables the identification of elevated levels of boundary layer  
45 pollution undetectable by near UV observations alone. In this paper we discuss the  
46 combined use of OMI, CALIOP and AIRS observations for the characterization of  
47 aerosol properties, and show an improvement in OMI aerosol retrieval capabilities.

48  
49 **1. Introduction**

50 Since the discovery of the near-UV capability of absorbing aerosols detection  
51 from space over a decade ago [*Hsu et al.*, 1996; *Herman et al.*, 1997; *Torres et al.*, 1998],  
52 the UV Aerosol Index (AI), calculated from observations by the Total Ozone Mapping  
53 Spectrometer (TOMS) family of sensors, and more recently by the Ozone Monitoring

54 Instrument (OMI), has been used to map the daily global distribution of UV-absorbing  
55 aerosols such as desert dust particles as well as carbonaceous aerosols generated by  
56 anthropogenic biomass burning and wild fires [*Herman et al.*, 1997], and volcanic ash  
57 injected in the atmosphere by volcanic eruptions [*Seftor et al.*, 1999]. The AI concept  
58 for aerosol detection has also been applied to other near-UV capable sensors such as  
59 GOME [*Gleason et al.*, 1998; *De Graaf et al.*, 2005a ], and SCIAMACHY [*de Vries et*  
60 *al.*, 2009; *De Graaf et al.*, 2005b].

61 In addition to the qualitative AI product, near-UV retrieval algorithms of aerosol  
62 extinction optical depth (AOD) and single scattering albedo (SSA) making use satellite  
63 measurement in the 330-388 nm range have been applied to the TOMS [*Torres et al.*,  
64 1998, 2002] and OMI [*Torres et al.*, 2007, *Ahn et al.*, 2008] observations. The quantitative  
65 interpretation of the near-UV measurements in terms of aerosol absorption, however, is  
66 affected by the dependency of the measured radiances on the height of the absorbing  
67 aerosol layer [*Torres et al.*, 1998; *De Graaf et al.*, 2005a], and the difficulty in  
68 differentiating between carbonaceous and desert dust aerosol types especially over land.

69 In the absence of direct observations to diagnose the location of the aerosol layer  
70 in the atmosphere the TOMS aerosol algorithm [*Torres et al.*, 2002] used a transport  
71 model generated climatology of aerosol layer height [*Ginoux et al.*, 2001]. To  
72 differentiate between absorbing aerosol types, the TOMS algorithm used geographical  
73 location and surface type considerations to prescribe the most likely absorbing aerosol  
74 type (carbonaceous or desert dust) present in the atmospheric column.

75 The near-simultaneity of satellite observations by a plurality of A-train sensors,  
76 provides the unprecedented opportunity of combining time and space collocated radiance

77 observations and/or derived atmospheric parameters for global climate analysis  
78 [*Anderson et al*, 2005]. Combined A-train measurements can also be used in inversion  
79 algorithms to further constrain retrieval conditions, and thus reduce the need of  
80 assumptions. CALIOP (Cloud-Aerosol Lidar with Orthogonal Polarization)  
81 measurements of the vertical distribution of the atmospheric aerosol load, and  
82 Atmospheric Infrared Sounder (AIRS) carbon monoxide (a reliable tracer of  
83 carbonaceous aerosols) observations, provide information that can be used to prescribe  
84 aerosol layer height and determine aerosol type in the OMI near UV aerosol algorithm  
85 (OMAERUV).

86 In this paper we discuss the use of observations by A-train sensors CALIOP and  
87 AIRS, on aerosol layer height and CO to provide reliable information on aerosol layer  
88 height and aerosol type as input to OMAERUV. In section 2, we briefly describe an  
89 improved version of the OMAERUV algorithm that utilizes CALIOP and AIRS  
90 observations as ancillary information. A detailed description of the way AIRS CO data  
91 is used in the OMI aerosol inversion procedure is presented in section 3, followed by a  
92 discussion of the development of a CALIOP-based aerosol layer height climatology in  
93 section 4, and an evaluation of the improved accuracy of OMI retrievals using  
94 AERONET observations in section 5. Summary and final remarks are presented in  
95 section 6.

96

## 97 **2. The OMAERUV Algorithm**

98 OMI is a spectrograph that measures upwelling radiances at the top of the  
99 atmosphere in the range 270-500 nm [*Levelt et al.*, 2006] since its deployment in 2004.

100 With a 2600 km across track swath and sixty viewing positions, it provided nearly daily  
101 global coverage at a 13x24 km nadir resolution (28x150 at extreme off-nadir) during the  
102 first three years of operation. Since mid-2007, an external obstruction to the sensor's  
103 field of view, perturbing OMI measurements of both solar flux and Earth shine radiance  
104 at all wavelengths, began to progressively develop. Currently, about half the sensor's  
105 sixty viewing positions are affected by what is referred to as 'row anomaly', since the  
106 viewing positions are associated with the row numbers on the CCD detectors. The site  
107 <http://www.knmi.nl/omi/research/product/rowanomaly-background.php> provides details  
108 on the onset and progression of the row anomaly.

109 The OMAERUV algorithm uses as input measured reflectances at 354 and 388  
110 nm to retrieve column atmosphere values of aerosol optical depth (AOD) and single  
111 scattering albedo (SSA). Ancillary information on near UV (354 and 388 nm) surface  
112 albedo ( $A_s$ ), surface type, and aerosol layer height (ALH) is required. Real time AIRS  
113 CO measurements are used to identify carbonaceous particles, and ALH is inferred  
114 based on CALIOP measurements. The way AIRS CO and CALIOP aerosol height  
115 information are used in the OMAERUV algorithm is the central theme of this paper, and  
116 it is discussed at length in sections 3 and 4.

#### 117 *-Aerosol models and forward calculations*

118 The algorithm assumes that the atmospheric aerosol column can be represented  
119 by one of three aerosol types: desert dust (*DD*), carbonaceous particles (*CB*), and sulfate-  
120 based (*SF*) aerosols. Each aerosol type is characterized by a fixed bi-modal spherical  
121 particle size distribution [*Torres et al., 2007*] with parameters derived from long-term  
122 AERONET statistics [*Dubovik et al., 2002*]. The relative spectral dependence of the

123 imaginary component of refractive in the 354-388 nm range,  $\Delta k$ , is assumed for each  
124 aerosol type [Torres *et al.*, 2007], and recently modified for the CB type to account for  
125 the absorption effects of organic carbon [Jethva and Torres, 2011]. Each aerosol type is  
126 further divided into seven sub-types to account for the variability of the imaginary  
127 component of the refractive index at 388nm,  $k_{388}$ , which, in combination with the  
128 assumed size distribution, translates into SSA variability.

129 Forward radiative transfer calculations of upwelling reflectance at the top of the  
130 atmosphere (354 and 388 nm) for the resulting 21 aerosol models were used to generate  
131 a set of look-up tables (LUT's) with nodal points in viewing geometry, aerosol optical  
132 depth (AOD), aerosol single scattering albedo (SSA), and aerosol layer height (ALH).

### 133 *-Inversion Procedure*

134 The measured reflectances are first used to calculate the scene 388 nm Lambert  
135 Equivalent Reflectivity ( $R_{388}$ ), and the absorbing Aerosol Index ( $AI$ ) as described in  
136 Torres *et al.* [2007]. To exclude sub-pixel cloud contamination effects, threshold values  
137 of the difference  $R_{388}-A_{388}$ , ( $\Delta R$ ), are used as upper limits in the allowed aerosol-related  
138 reflectivity increases beyond the value of the surface reflectance  $A_{388}$ .

139 Figure 1 shows a schematic overview of OMAERUV's retrieval procedure. At  
140 each OMI pixel, the  $AI$ ,  $COI$  (i.e., normalized CO column amount), and surface type  
141 (source: <http://www-surf.larc.nasa.gov/surf/pages/data-page.html>) are used to select an  
142 aerosol type. For simplicity, we define the dimensionless parameter  $COI$  ( $CO$  index) as  
143 the column  $CO$  amount (in molecules-cm<sup>-2</sup>) divided by 10<sup>18</sup> molecules-cm<sup>-2</sup>.

144 The absorbing aerosol type identification is achieved by examining the values of  
145  $AI$  and  $COI$  in relation to threshold values  $AI_0$  and  $COI_0$ , that represent respectively  $AI$

146 noise and background  $COI$  values not necessarily associated with the free troposphere  
147  $CO$  burden which is expected to co-exist with the lofted carbonaceous aerosols. The  
148 adopted values of  $COI_0$  are 2.2 and 1.8 for the northern and southern hemisphere  
149 respectively. The value of  $AI_0$  is 0.8 for both land and ocean conditions. As shown  
150 schematically in the upper-left panel of Figure 1, the presence of carbonaceous aerosols is  
151 assumed if  $AI \geq AI_0$  and  $COI \geq COI_0$ , or for  $COI > 2.8$  (2.5 in the southern hemisphere)  
152 regardless of  $AI$  considerations. On the other hand, when  $AI \geq AI_0$  and  $COI < COI_0$  desert  
153 dust aerosols are assumed present. If neither set of conditions are met the presence of  
154 sulfate aerosols is assumed.

155 Screening of sub-pixel cloud contamination is carried out making use of  $AI$ ,  $\Delta R$   
156 , and the selected aerosol type in an algorithm flagging scheme that assigns confidence  
157 levels on the occurrence of cloud-free conditions as shown on the upper right box of  
158 Figure 1. This is done by means of an algorithm Quality Flag (QF) whose value is 0 for  
159 minimum cloud presence, and has a value of 1 when it is suspected that the retrieval  
160 product is affected by cloud contamination.

161 Different retrieval approaches are applied over the oceans and the continents.  
162 Over the oceans, the retrieval is only carried out when either DD or CB aerosols are  
163 present as indicated by the  $AI$  parameter. No retrieval takes place over the oceans for  $AI$   
164 values less than 0.8. Retrievals over land, on the other hand, are carried out under all  
165 conditions regardless of the value of  $AI$ . The actual retrieval method depends on the  
166 nature of the aerosol signal as indicated by the magnitude of the  $AI$  and  $COI$  parameters.  
167 A two-channel method that allows the simultaneous retrieval of AOD and SSA, or, a  
168 single-channel retrieval of AOD is applied depending on aerosol type and  $AI$

169 considerations as shown on the lower right box of Figure 1. When the single-channel  
170 approach is applied, a SSA of 1.0 is assumed. Retrievals results are obtained for the  
171 five ALH nodal point in in the LUT's (surface, 1.5, 3, 6, and 10 km).

172 A best-guess aerosol layer height must be prescribed as the accuracy of the  
173 satellite retrieved properties of absorbing aerosol types in the near UV, is highly  
174 sensitive to the aerosol layer altitude above the ground [Torres *et al.*, 1998]. The lower  
175 left diagram of Figure 1 describes the steps for ALH determination. For the SF aerosol  
176 type, a vertically decaying distribution is used, in which aerosol concentration is largest  
177 at the surface and decreases exponentially with height. If either the DD or CB aerosol  
178 type has been selected, the best guess ALH is given by a CALIOP-based  
179 climatological value ( $Z_{clp}$ ) developed for this purpose, and discussed in detail in section 4.  
180 If the CALIOP climatology does not provide an ALH entry, an ALH assumption is made  
181 that depends on aerosol type and location as shown in Fig 1. Carbonaceous aerosols  
182 layers within 30° of the Equator are assumed to have maximum concentration at 3 km  
183 above the surface whereas mid and high-latitude (pole wards of  $\pm 45^\circ$ ) smoke layers are  
184 assumed to peak at 6 km. The height of smoke layers between 30° and 45° latitude in both  
185 hemispheres is interpolated with latitude between 3 and 6 km. The location of desert dust  
186 aerosol layers varies between 1.5 and 10 km, and is given by a multiyear climatological  
187 average of Chemical Model Transport (CTM) calculations using the GOCART model  
188 [Ginoux *et al.*, 2001] gridded at a resolution of 2.5°. Thus, in addition to retrievals at five  
189 standard ALH values, a retrieval at the best-guess value of ALH is also reported.

190

### 191 **3. Combined use of OMI-AI and AIRS-CO for aerosol type identification**



192 In the near-UV, the separation between absorbing and non-absorbing aerosol  
193 types is straightforward given the large sensitivity to aerosol absorption in this spectral  
194 region. Differentiating between carbonaceous (fine particles) and dust (coarse particles)  
195 aerosols in ocean satellite retrieval algorithms that use visible and near IR observations is  
196 generally done in terms the well known Angstrom's wavelength exponent (AE)  
197 [Angstrom, 1929], whose magnitude is inversely related to the predominant particle size.  
198 Typical AE values vary from nearly zero for high concentrations of desert dust aerosols  
199 to values of 2.0 or greater associated with large AOD fine size carbonaceous aerosols  
200 [Eck et al., 1999; Toledano et al., 2011]. Satellite derived AE for aerosol type  
201 differentiation over land is unreliable due to uncertainties associated with surface  
202 reflectance characterization [Levy et al., 2010]. Because of the short separation of the two  
203 channels in the OMAERUV algorithm, the AE concept is not applicable and, therefore,  
204 distinguishing between fine and coarse size mode absorbing aerosol types (i.e.,  
205 carbonaceous versus desert dust aerosols) requires additional external information.  
206 Although OMI reflectance measurements up to 500 nm are available their use in AE  
207 calculation require a precise characterization of visible surface albedo currently  
208 unavailable.

### 209 *3.1 Carbonaceous Aerosols Tracers*

210 Nitrogen dioxide ( $NO_2$ ) and formaldehyde ( $HCHO$ ) are important biomass  
211 burning byproducts measured by OMI that could be used as carbonaceous aerosol  
212 tracers. Because of their relative short lifetimes (only up to a few hours) , however, these  
213 trace gas are not adequate for tracing the long-range aerosol transport . Carbon monoxide  
214 ( $CO$ ), on the other hand, is the second most abundant trace gas produced by biomass

215 burning [Sinha et al., 2003], and has a multiday-long lifetime that makes it a suitable  
216 tracer of long-range transport carbonaceous aerosols. Luo et al. [2010], found a clear  
217 spatial correlation between Tropospheric Emission Spectrometer (TES) CO  
218 measurements and the OMI Aerosol Index signal of the smoke plume generated by the  
219 2006 Australian fires [Torres et al., 2007, Dirksen et al., 2009]. Satellite global daily CO  
220 measurements are routinely produced by the Measurements of Pollution in the  
221 Troposphere (MOPITT) sensor on the Terra satellite [Pan et al., 1998] and by the  
222 Atmospheric Infrared Sounder (AIRS) on the Aqua platform [Aumann et al., 2003].  
223 Because of the near-simultaneity of AIRS and OMI observations, the AIRS CO product  
224 is used in this analysis.

### 225 3.2 The AIRS CO product

226 The AIRS sensor was deployed on May 4, 2002. It is a cross-track scanning  
227 grating spectrometer that measures IR radiation at 2378 channels between 3.7 and 16  $\mu\text{m}$   
228 with a 13.5 km nadir field of view [Aumann et al., 2003]. AIRS' CO inversion uses  
229 radiances in the 4.50-4.58  $\mu\text{m}$  region. It is considered a robust retrieval because of its  
230 strong spectral signature and weak water vapor interference with an estimated accuracy  
231 of about 15% [McMillan et al., 2005]. The use of cloud-clearing [Chahine et al, 1974]  
232 allows the retrievals of global CO for conditions up to 80% cloudy [Suskind et al, 2003].  
233 In this analysis we used the global daily gridded AIRS column CO product expressed as  
234 molecules-cm<sup>-2</sup> at a 1°x1° resolution, available at <http://daac.gsfc.nasa.gov/AIRS> .

### 235 3.3 Combined use of CO and AI observations

236 The spatial distributions of tropospheric CO amounts and atmospheric load of  
237 carbonaceous aerosols are naturally correlated as both species are generated by biomass

238 burning. On the other hand, no correlation is expected to exist between tropospheric *CO*  
239 and the atmospheric aerosol burden associated with desert dust particles. An example of  
240 the expected relationship between *CO* and dust and smoke aerosols is shown in Figure 2.  
241 The top panel shows the global spatial distribution of the OMI *AI* on July 7, 2006. The  
242 *AI* map shows pools of large *AI* values over Southeastern Canada and Eastern US  
243 possibly associated with an advancing smoke layer generated by boreal fires in Canada.  
244 Another large absorbing aerosol plume lingers over Equatorial Africa between the  
245 Equator and about 10°S, most likely the result of agriculture-related burning practices.  
246 Large *AI* values are also present over the arid areas of Northern Africa, the Arabian  
247 Peninsula, and Central Asia, as well as over the Atlantic Ocean indicating the presence  
248 of a drifting synoptic scale desert dust plume. The center panel in Fig. 2 shows the  
249 AIRS-*CO* column amount as derived from AIRS observations on the same day. Note  
250 that very large values of *CO* column amounts are observed over the areas dominated by  
251 the presence of smoke but not over the large regions occupied by the desert dust layers.  
252 The combined use of the *AI* and *COI* (as defined in section 2) parameters allows the  
253 separation of smoke/dust plumes as shown on the bottom panel of Fig. 2.

254         Although this straightforward way of separating absorbing aerosol types works  
255 very well in most cases, it may break down under certain circumstances. A notable case  
256 when the approach fails, takes place when dust aerosols are present over a region  
257 characterized by high *CO* levels associated with pollution episodes other than smoke. In  
258 this case the above described approach will identify the absorbing aerosol type as smoke.  
259 This situation is likely to happen over Eastern China during the spring season when the

260 normally high *CO* levels co-exist with the westerly flow of large amounts of desert dust  
261 aerosols from the Gobi and Taklimakan deserts.

262 The *CO*-based aerosol type separation technique is particularly useful to pick up  
263 the presence of drifting layers of carbonaceous aerosols over arid areas. One such event  
264 took place on 27 August 2007 when the smoke plume of the fires in Greece moved south  
265 across the Mediterranean reaching Northern Libya and Algeria [*Turquety et al.*, 2009].  
266 The aerosol type map in Fig 3., obtained by the previously described method, shows the  
267 unmistakable presence of the Greek fires smoke plume over Northern Africa.

### 268 *3.4 Boundary Layer Pollution Aerosols*

269 *CO* measurements are also used in the OMAERUV algorithm to indentify cases  
270 of high amounts of carbonaceous aerosols in the boundary layer that would otherwise go  
271 undetected by the *AI*. Large summer AOD values are reported by AERONET  
272 observations in rapidly developing industrial regions of the world such as northeastern  
273 China and northern India. Because of their low elevation these aerosols yield *AI* values  
274 below the reliability limit ( $\sim 0.8$ ) in the near UV. In addition, because of their  
275 extraordinarily large concentrations they were often mistaken as cloud contamination in  
276 earlier versions of the algorithm. Correlative analysis of ground-based AOD  
277 measurements and satellite *CO* measurements (not shown) indicate high correlation  
278 between the two parameters. Based on this analysis OMAERUV retrievals are now  
279 carried out when the measured *CO* values are larger than  $2.8E18$  (NH) or  $2.5E18$  (SH)  
280 regardless of the *AI* value.

281

## 282 **4. Combined use of OMI and CALIOP observations**

283 CALIOP is a three-channel lidar on board the CALIPSO platform launched in  
284 April 28, 2006 in an ascending polar orbit with a 1:32 pm Equator crossing time. It  
285 measures polarization insensitive attenuated backscatter at 532 and 1064 nm during both  
286 day and night time. In addition, CALIOP measures polarization sensitive backscatter at  
287 532 nm. CALIOP probes the atmosphere between the surface and 40 km above sea level  
288 at a vertical resolution that varies between 30 and 60 m. The horizontal resolution along  
289 the orbital track is 335 m [*Winker et al.*, 2009]. CALIOP data is available since mid-June  
290 2006 and, except for minor interruptions, continues to be available to present. In addition  
291 to the attenuated backscatter profile data, CALIOP's aerosol products includes a Vertical  
292 Feature Mask that characterizes particle layers as either cloud or any of several aerosol  
293 types, and an aerosol optical depth product. In this study we use daytime observations of  
294 the 1064 nm attenuated backscatter. Unlike AIRS global daily coverage, CALIOP's  
295 narrow 335 m footprint does not allow the direct use of daily observations as no global  
296 coverage is available. Therefore, developing a climatological data set is the best way to  
297 make use of CALIOP provided aerosol layer height data.

#### 298 *4.1 Collocation*

299 The OMI sensor makes observations at sixty positions (or viewing angles) across  
300 the orbital track. Positions 30 and 31 are closest to nadir. At launch, CALIPSO's sub-  
301 satellite point coincided with OMI's scan position 45 on the right side of the OMI scan  
302 for most of the orbit at low and mid-latitudes, and the time difference between OMI and  
303 CALIOP daytime observations was about 13 minutes. As the Aura satellite orbit was  
304 changed to reduce the overpass time difference with that of Aqua, the OMI scan position  
305 of coincidence with CALIOP's observations changed to 37 over several months, and by

306 the end of the orbital maneuver the time observation difference between CALIOP and  
307 OMI decreased to about 7 minutes.

308 At the 335 m CALIOP's horizontal resolution, there are 39 CALIOP profiles of  
309 attenuated backscatter per OMI-CALIOP collocation pixel (OCCP) along CALIPSO's  
310 orbital track. In this work we use a specially created set of orbital files that contain  
311 merged OMI and CALIOP data collocated along CALIPSO's orbital track. The OMI  
312 level 2 data subset coincident with CALIOP's measurements was produced by the A-  
313 Train Data Depot (ATDD) project at the Goddard Earth Sciences Data and Information  
314 Services Center to address the differences in spatial, vertical, and horizontal, as well as  
315 temporal scales of coverage of different instruments participating in the A-Train  
316 [Savtchenko *et al.*, 2008]. The ATDD data set was augmented with CALIOP's  
317 observations of attenuated backscatter at 532 and 1064 nm. In addition to the CALIOP  
318 backscatter data and ancillary information, the merged orbital files contain OMI  
319 measured radiances, viewing geometry, ancillary data and original retrieval results at the  
320 OCCP plus four additional OMI pixels on each side of the OCCP for a total of 9 pixels.

321

#### 322 *4.2 Cloud Screening*

323 The available CALIOP backscatter profiles per OCCP were combined to create an  
324 average profile representative of the vertical distribution of the atmospheric load of  
325 carbonaceous and/or desert dust aerosols over the OCCP. An attempt to minimize the  
326 effect of cloud contamination on both observations was carried out by applying cloud  
327 screening procedures to both OMI and CALIOP observations as described by *Chen et al*  
328 [2012]. Heavily cloud contaminated OMI data was excluded by rejecting observations

329 where the OCCP derived Lambert Equivalent Reflectivity (LER) was larger than 25%.  
330 The calculated average CALIOP profiles were screened for the presence of clouds by  
331 excluding those layers where the resulting average backscatter was larger than 0.005. The  
332 effect of noise was also excluded by rejecting layers where average backscatter was  
333 smaller than 0.0015. Figure 4 shows CALIOP's average attenuated backscatter profiles  
334 associated with a carbonaceous aerosol layer in South America (left panel), and a desert  
335 dust layer in Northern Africa (right panel) calculated using both 532 and 1064 nm  
336 CALIOP observations. While no apparent difference in sensitivity between the 532 and  
337 1064 channels is observed for desert dust particles (right panel), it appears that in the  
338 presence of biomass burning aerosols (left panel) the 532 nm measurement loses  
339 sensitivity to aerosols near the surface. If low level aerosols are not accounted for, the  
340 derived aerosol layer altitude would be biased high. For that reason, in this analysis we  
341 use CALIOP's 1064 nm measurements that are sensitive to the presence of carbonaceous  
342 and desert dust aerosols all the way to the surface.

343

#### 344 *4.3 Aerosol layer height calculation*

345 In reducing the CALIOP measured profiles, it was assumed that the vertical  
346 structure of the tropospheric aerosol load can be represented as a single layer of  
347 height  $ALH$ . This assumption seeks to facilitate the use of the resulting climatology as  
348 input to global retrieval algorithms. Although, multiple aerosol layers are common,  
349 elevated dust or carbonaceous particles are most frequently observed as single layers.  
350 The parameter  $Z_{aer}$  was calculated as the attenuated-backscatter-weighted height  
351 according to the expression

352 
$$Z_{aer} = \sum_{i=1}^n H(i) \left[ \frac{B_{sc}(i)}{\sum_{i=1}^n B_{sc}(i)} \right] \quad (1),$$

353 where  $B_{sc}(i)$ , is the attenuated backscatter at height  $H(i)$ , and  $n$  is the number of layers  
 354 between the surface and 10 km. The resulting aerosol layer height was assumed to be  
 355 representative of the aerosol layer altitude at the OCCP. The information on aerosol layer  
 356 height at the fine CALIOP resolution was propagated a few hundred meters beyond the  
 357 OCCP. The aerosol layer height at the OCCP was also assumed to be representative of  
 358 the aerosol altitude at any pixel in the nine-OMI-pixel subset (i.e., within approximately  
 359 100 km of the OCCP in the same swath) if the presence of dust or smoke was detected  
 360 according to the *AI*. By the same token, if for an OCCP pixel the CALIOP height was  
 361 undetermined (due to excessive cloud contamination) but the *AI* on other non-OCCP  
 362 pixels in the same swath indicated aerosol presence the height for the corresponding  
 363 pixel-position from the previous across-track-scan was assumed if available. It should  
 364 be emphasized that the resulting aerosol height data set is not a general representation of  
 365 the altitude of all aerosol types but it is specifically designed to account for the height of  
 366 elevated carbonaceous and desert dust aerosol layers when present.

367 Figure 5 shows three examples of the resulting aerosol layer height derived from  
 368 1064 nm CALIOP measurements as previously described. The solid line indicates the  
 369 effective aerosol layer height calculated using equation (1), and the dashed line  
 370 represents the aerosol layer height assumed in the previous version of OMAERUV  
 371 algorithm [Torres *et al.*, 2007]. CALIOP's observed vertical structure of the aerosol load  
 372 on April 4, 2007 near the Bodele depression in the Central Saharan desert shows the  
 373 unmistakable signature of a rising column of dust between the surface and about 3 km at



374 16°N, 12°E is shown on the top panel of Figure 5. The airborne dust plume spreads north  
375 and south of the source in an atmospheric layer between 3 and 5 km. The aerosol layer  
376 height assumed in the OMAERUV algorithm is underestimated by as much as 2 km in  
377 relation to that inferred from CALIOP observations.

378 The center panel illustrates the vertical structure of a smoke layer as seen by the  
379 CALIPSO lidar on August 12, 2006 over Angola and Namibia, and the Southern Atlantic  
380 Ocean. CALIOP observations show the westward flow of smoke from fires in Angola  
381 and Namibia over the Southern Atlantic Ocean. The CALIOP curtain image shows a  
382 south-north transect of the smoke layer along the western coast of Central Africa from  
383 Angola, covering Angola's coastal waters (~12°S, 13°E), and reaching land again over  
384 the republic of Congo's coastal area (~5°S, 11.5E). Over the central and northern sections  
385 of the transect, the aerosol layer is clearly located above low clouds. . The smoke layer  
386 over land generated from fires in Angola and Namibia occupies a 2.5 km thick layer that  
387 goes from the surface (about 1 km above sea level) to 3.5 km as indicated by the  
388 attenuated backscatter signal. The assumed aerosol layer height is consistently higher  
389 than the CALIOP derived value.

390 A layer of carbonaceous aerosols as seen by the OMI and CALIOP sensors over  
391 Central Brazil on September 30, 2007 is depicted on the bottom panel of Fig 5. The  
392 CALIOP curtain plot depicts the vertical structure of the layer over a region between  
393 10°S and 30°S along CALIOPS's orbital track. On the northern most end of the plume,  
394 the aerosol load is located in a 1 km thick layer between 3 and 4 km above the ground,  
395 and widens towards the south. In general, the assumed height is about 1 km higher than  
396 the CALIOP-based estimate.

397

#### 398 4.4 CALIOP-based aerosol height climatology

399 The procedure described in the previous section to derive an effective aerosol  
400 layer height was applied to the global CALIOP record over the two year period from  
401 July 2006 to December 2008. The extension beyond 2008 was hindered by the loss of the  
402 OCCP resulting from the onset of the OMI row anomaly discussed in section 2. Gridded  
403  $1^\circ \times 1^\circ$  resolution monthly averages of *ALH* were calculated. A minimum of five data  
404 points per-grid were required to produce a monthly value. Extracts from a degraded  $5^\circ \times 5^\circ$   
405 gridded product was used to fill gaps in the original  $1^\circ \times 1^\circ$  product resulting from  
406 CALIOP's lack of global coverage and the interference of clouds. Additionally, image  
407 processing techniques using convolution and Gaussian smoothing [*Gonzalez and Woods,*  
408 1992] were applied to reduce the noise and minimize the effect of isolated maxima and  
409 minima.

410 Figure 6 shows global maps of the monthly averaged aerosol layer height ( $Z_{clp}$ ),  
411 in km above surface, derived from CALIOP observations. Maps shown correspond to the  
412 mid-season months (January, April, July, October).

413 The  $Z_{clp}$  spatial distribution in January is dominated by the presence of desert dust  
414 and carbonaceous aerosols copiously produced by their emission sources in the Saharan  
415 (desert dust) and Equatorial Africa (biomass burning).  $Z_{clp}$ 's between 3 and 4 km  
416 predominate over the northern African deserts, while values between 2 and 3 km are  
417 observed associated with the fire activity in the tropical belt along the Atlantic coast  
418 from Guinea to Nigeria, and extending eastwards to Ethiopia. Over the northern Atlantic  
419 Ocean,  $Z_{clp}$  descends rapidly westwards from over 2 km at the Northern African West

420 coast to the 45°W meridian, and continues to decrease, with some oscillations, to  
421 minimum values of about 1 km over the Gulf of Mexico.  $Z_{clp}$ 's around 3 km can be  
422 observed over the SE United States as a consequence of local fires, as well as long range  
423 transport from Central America. High  $Z_{clp}$  values are also observed in the Southern  
424 Hemisphere Summer over the land masses of South America (Patagonia), Western  
425 Africa, and Australia where desert dust production and smoke from brush fires  
426 (Australia) are commonly observed in January.

427         A significant narrowing in the  $Z_{clp}$  north-south distribution over the Atlantic  
428 Ocean is apparent in Spring following the conclusion of the Equatorial Africa biomass  
429 burning season.  $Z_{clp}$  values higher than those observed in winter are apparent over the  
430 Atlantic Ocean owing to the Spring activation of Saharan dust sources. Elevated layers  
431 (3km and higher) can be observed over the eastern half of the continental US, generally  
432 resulting from the transport of carbonaceous aerosols from boreal wild fires in Canada  
433 (northeast) and local sources, as well as contribution from transport from Mexico and  
434 Central America (southeast). The observed  $Z_{clp}$ 's lower than 3 km over the western half  
435 of the US are likely associated with local dust production. As a consequence of the  
436 activation of dust sources in Central Asia, elevated layers ( 3km and higher) are apparent  
437 over Afghanistan, Turkmenistan, and Uzbekistan. Long range transport of desert dust  
438 from the Saharan sources across the Mediterranean, and from sources in Central Asia  
439 trigger the spread of dust aerosol layers about 2.5 km high over western and northern  
440 Europe. Eastward transport of desert dust following the Spring activation of the Gobi  
441 and Taklamakan deserts, and layers of carbonaceous aerosols from biomass burning in  
442 Southeast Asia linger over East Asia in layers 2 to 3 km high .

443 An enhanced Summer  $Z_{clp}$ , associated with the northward spread of aerosol  
444 layers from boreal fires in Canada and Siberia, is observed at about 3 km. The Summer  
445 Saharan aerosol layer over the Atlantic Ocean between 10°N and 30°N varies in altitude  
446 between 3.5-40 km at the West Coast of Northern Africa going down towards the West,  
447 reaching 1.5 km over the Gulf of Mexico. Smoke from biomass burning activity in  
448 Central Africa spills over the Southern Atlantic Ocean in an aerosol layer at 2-2.5 km.

449 The Autumn global aerosol height distribution is characterized by an overall  $Z_{clp}$   
450 decrease. Except for a height increase over the biomass burning regions in the Southern  
451 Hemisphere, Autumn  $Z_{clp}$  values are lower than the previous season values by 1 - 2 km  
452 over most of the globe. The Saharan Layer  $Z_{clp}$  over the Atlantic Ocean reaches values as  
453 low as 1.5 km about halfway between Northern Africa and the Gulf of Mexico. The  
454 carbonaceous aerosol layer, known as the 'river of smoke', flowing off Southeast Africa  
455 along the Indian Ocean at a 1~2 km height  $Z_{clp}$  is clearly observed .

456

## 457 **5. Evaluation of improvements in OMAERUV retrievals**

458 A brief discussion of the effect of the algorithm upgrades on retrieved products  
459 is presented here. Comprehensive assessments of the OMAERUV products using  
460 ground based and other satellite observations are discussed in detail by *Ahn et al.* [2013]  
461 and *Jethva et al.* [2013].

462 The effect of using the CALIOP  $Z_{clp}$  climatology as input in the OMI inversion  
463 algorithm, was evaluated by comparing the optical depth from the OMAERUV algorithm  
464 to AERONET observations using both the standard algorithm aerosol height assumption  
465 and the aerosol altitude extracted from the CALIOP climatology described here. The

466 assessment exercise was carried out using AERONET measurements at the five sites  
467 listed in Table 1, where the presence of elevated dust and smoke layers is routinely  
468 observed. Columns 4 through 8 in Table 1 show respectively the resulting correlation  
469 coefficient ( $r$ ), intercept, the rms, and the number of retrievals within 10% ( $Q_{10}$ ) and 30%  
470 ( $Q_{30}$ ) of the AERONET values, for both the standard aerosol layer height assumption,  
471 and the CALIOP provided height information. The standard OMAERUV method of  
472 prescribing aerosol layer height of desert dust layers based on a model-generated  
473 climatology works fairly well as indicated the correlation coefficients between 0.71 and  
474 0.83 at the five locations. Small but important improvement in these statistics is obtained  
475 when the CALIOP-based climatology of aerosol layer height. The CALIOP-based  
476 approach yields higher correlation coefficients (between 0.74 and 0.84) and slightly  
477 smaller intercepts. The improvement is noticeable in terms of the  $Q_{10}$  and  $Q_{30}$  parameters,  
478 defined as the number of points (in percent) within 10% and 30% of the ground truth  
479 observations.  $Q_{10}$  went up between 3 and 17% at the five sites whereas  $Q_{30}$  increased  
480 between 3% and 11%. In most cases the effect of using the CALIOP-based aerosol layer  
481 height was to reduce AERONET-OMI differences in the winter season when the aerosol  
482 layer height is under-estimated by the standard assumption. The observed improvement is  
483 smallest in the middle of the Saharan Desert (Tamanrasset site) and increases rapidly  
484 away from the dust aerosol source areas with the largest improvement registered at  
485 Dakar. The scatter plot in Figure 7 illustrates the resulting OMAERUV AOD  
486 improvement in relation to AERONET observations at the Banizoumbou AERONET  
487 site.

488           As illustrated in Figure 3, the use of CO measurements as an aerosol tracer has  
489 facilitated the identification of carbonaceous aerosols over arid regions, where the  
490 distinction between dust and smoke particles would not have been possible without the  
491 availability of CO observations. The AIRS CO data has also enabled the detectability  
492 and characterization of high levels of boundary layer pollution aerosols undetectable by  
493 the previous OMAERUV algorithm without the help of AIRS CO data. Figure 8 depicts  
494 the retrieved fields of aerosol optical and single scattering albedo on August 20, 2007  
495 over Northeastern China by the previous (top) and current (bottom) versions of the  
496 algorithm.

## 497 **6. Summary and Conclusions**

498           We have documented the use of CALIOP aerosol vertical distribution  
499 information and AIRS CO column amounts to provide information on aerosol layer  
500 height and aerosol type necessary for the retrieval of AOD and SSA by the OMAERUV  
501 algorithm. The combined use in real time of observations from sensors on two different  
502 satellites is only possible thanks to the near-simultaneity of A-train observations.

503

504           It has been shown that the combined use of AIRS CO observations and the OMI  
505 UV aerosol index provides a way of reliably identifying the absorbing aerosol type when  
506 absorbing aerosols have been positively detected via the AI. Because CO is an excellent  
507 tracer of carbonaceous aerosols, elevated values of both AI and CO correspond in most  
508 cases to the presence of smoke layers whereas the occurrence of high AI values and low  
509 CO amounts is associated with layers of desert dust aerosols. Another useful application  
510 of the AIRS CO data is the identification of high boundary layer aerosol loads that would

511 otherwise be dismissed as cloud contamination by OMAERUV. Because of the large  
512 aerosol load associated with these events over biomass burning regions and Eastern  
513 China, it is possible to retrieve both aerosol optical depth and single scattering albedo.

514

515 We made use of time and space collocated CALIOP and OMI observations for  
516 the determination of the height of elevated layers of carbonaceous and desert dust  
517 aerosols detected by OMI's near UV observations. An effective aerosol layer height was  
518 calculated as the attenuated-backscatter-weighted average height obtained from  
519 CALIOP's 1064 nm measurements. Observations at 1064 nm were chosen over the 532  
520 nm measurements because of apparent saturation effects at the shorter wavelength. The  
521 OMI-CALIOP combined analysis was carried out over a 30-month record from July-  
522 2006 to December 2008, when instrumental issues affecting the OMI sensor resulted in  
523 the loss of the collocation capability.

524 A 30 month climatology of aerosol layer height was calculated. The impact of  
525 using CALIOP-based climatology of aerosol layer height was evaluated by comparing  
526 OMI retrieved AOD's to AERONET observations at a number of locations in Northern  
527 Africa. Validation results indicate that although previous algorithm assumptions on  
528 aerosol layer height worked reasonably well, the use of the CALIOP-based climatology  
529 produces a noticeable improvement of retrieval results. The CALIOP-based absorbing  
530 aerosol layer height climatology and the real-time use of AIRS CO observations have  
531 been integrated into the current version of the OMAERUV algorithm.

532

533 **References**

- 534 Ahn, C., O. Torres, and H. Jethva (2013), Assessment of OMI near UV Aerosol Products.  
 535 Part 1: Evaluation of Aerosol Optical Depth (*submitted*)
- 536 Ahn C., O. Torres, and P.K. Bhartia (2008), Comparison of OMI UV Aerosol Products  
 537 with Aqua-MODIS and MISR observations in 2006, *J. Geophys. Res.*, 113, D16S27,  
 538 doi:10.1029/2007JD008832
- 539 Anderson, T.L., R.J. Charlson, N. Bellouin, O. Boucher, M. Chin, S.A. Christopher, J.  
 540 Haywood, Y. J. Kaufman, S Kinne, J. A. Ogren, L.A. Remer, T. Takemura, D. Tanre,  
 541 O. Torres, C.R. Trepte, B.A. Wielicki, D.M. Winker, and H. Yu, Am “A-Train”  
 542 Strategy for Quantifying Direct Climate Forcing by Anthropogenic Aerosols, *Bull.*  
 543 *Amer. Met. Soc.*, December, 2005
- 544 Angstrom, A. (1929), On the atmospheric transmission of Sun radiation and on dust in  
 545 the air, *Geogr. Ann.*, 12, 130-159.
- 546 Aumann, H. H., et al. (2003), AIRS/AMSU/HSB on the Aqua mission: Design, science  
 547 objectives, data products, and processing systems, *IEEE Trans. Geosci. Remote Sens.*,  
 548 41, 253–264.
- 549 Chahine, M. T. (1974), Remote sounding of cloudy atmospheres, I, The single cloud  
 550 layer, *J. Atmos. Sci.*, 31, 233– 243.
- 551 Chen, Z., O. Torres, M.P. McCormick, W. Smith, and C. Ahn (2012), Comparative  
 552 Study of aerosol and cloud detected by CALIPSO and OMI, *Atmos. Environ.*, 51,  
 553 187-195.
- 554 De Graaf, M., P. Stammes, O. Torres, and R.B.A. Koelemeijer (2005a), Absorbing  
 555 Aerosol Index: Sensitivity Analysis, Application to GOME and Comparison with  
 556 TOMS, *J. Geophys. Res.*, 110, D01201, doi:10.1029/2004JD005178
- 557 De Graaf, M. and Stammes, P., (2005b), SCIAMACHY Absorbing Aerosol Index –  
 558 Calibration issues and global results from 2002–2004, *Atmos. Chem. Phys.*, 5, 2385–  
 559 2394
- 560 de Vries Penning, M. J. M., Beirle, S., and Wagner, T. (2009), UV Aerosol Indices from  
 561 SCIAMACHY: introducing the SCattering Index (SCI), *Atmos. Chem. Phys.*, 9, 9555-  
 562 9567, doi:10.5194/acp-9-9555-2009.
- 563 Dirksen, R. J., K. Folkert Boersma, J. de Laat, P. Stammes, G. R. van der Werf, M. Val  
 564 Martin, and H. M. Kelder (2009), An aerosol boomerang: Rapid around-the-world  
 565 transport of smoke from the December 2006 Australian forest fires observed from  
 566 space, *J. Geophys. Res.*, 114, D21201, doi:10.1029/2009JD012360.
- 567 Dubovik, O., B. Holben, T.F. Eck, A. Smirnov, Y.J. Kaufman, M.D. King, D. Tanre, and  
 568 I. Slutsker (2002), Variability of absorption and optical properties of key aerosol types  
 569 observed in worldwide locations, *J. Atm. Sci.*, 59, 590-608.
- 570 Eck, T.F., B.N. Holben, J.S. Reid, O. Dubovik, A. Smirnov, N.T O'Neill, I. Slutsker, and  
 571 S. Kinne (1999), Wavelength dependence of the optical depth of biomass burning,  
 572 urban and desert dust aerosols, *J. Geophys. Res.*, 104, D24, 31333–31349.
- 573 Ginoux, P., M. Chin, I. Tegen, J. M. Prospero, B. Holben, O. Dubovik, and S.-J. Lin  
 574 (2001), Sources and distributions of dust aerosols simulated with the GOCART  
 575 model, *J. Geophys. Res.*, 106(D17), 20255–20273, doi:10.1029/2000JD000053.



576 Gleason, J., N.C. Hsu and O. Torres, (1998), Biomass burning smoke measured using  
577 backscattered ultraviolet radiation: SCAR-B and Brazilian smoke inter annual  
578 variability, *J. Geophys Res.*, 103, 31969-31978  
579 Gonzalez R., and R. Woods (1992), *Digital Image Processing*, Addison-Wesley  
580 Publishing Company, , p 191.  
581 Herman, J.R., P.K. Bhartia, O. Torres, C. Hsu , C. Seftor, and E. Celarier (1997), Global  
582 Distribution of UV-absorbing Aerosols From Nimbus-7/TOMS data, *J. Geophys. Res.*,  
583 102, 16911-16922  
584 Hsu, N.C., J.R. Herman, P.K. Bhartia, C.J. Seftor A.M. Thompson, J.F. Gleason, T.F.  
585 Eck, and B. N. Holben (1996), Detection of biomass burning smoke from TOMS  
586 measurements, *Geophys. Res. Lett.*, 23, 745-748.  
587 Jethva, H., O. Torres and C. Ahn (2013), Assessment of OMI near UV Aerosol Products.  
588 Part 2: Comparison of Single Scattering Albedo to Ground-Based AERONET  
589 Observations in Biomass Burning and Dust Environments (*submitted*)  
590 Jethva, H. and O. Torres (2011), Satellite-based evidence of wavelength-dependent  
591 aerosol absorption in biomass burning smoke inferred from Ozone Monitoring  
592 Instrument, *Atmos. Chem. Phys.*, 11, 10541-10551, doi:10.5194/acp-11-10541-201.  
593 Levelt, P. F., E. Hilsenrath, G. W. Leppelmeier, G. H. J. van den Ooord, P. K. Bhartia, J.  
594 Tamminen, J. F. de Haan, and J. P. Veeffkind (2006), Science objectives of the Ozone  
595 Monitoring Instrument, *IEEE Trans. Geosci. Remote Sens.*, 44(5), 1093–1101.  
596 Levy, R. C., Remer, L. A., Kleidman, R. G., Mattoo, S., Ichoku, C., Kahn, R., and  
597 Eck, T. F., (2010), Global evaluation of the Collection 5 MODIS dark-target aerosol  
598 products over land, *Atmos. Chem. Phys.*, 10, 10399-10420, doi:10.5194/acp-10-  
599 10399-2010.  
600 Luo, M., C. Boxe, J. Jiang, R. Nassar, and N. Livesey, (2010), Interpretation of Aura  
601 satellite observations of CO and aerosol index related to the December 2006 Australia  
602 fires, *Remote Sensing of Environment*, 114, 2853-2862.  
603 McMillan, W. W., C. Barnet, L. Strow, M. T. Chahine, M. L. McCourt, J. X. Warner, P.  
604 C. Novelli, S. Korontzi, E. S. Maddy, and S. Datta (2005), Daily global maps of  
605 carbon monoxide from NASA's Atmospheric Infrared Sounder, *Geophys. Res. Lett.*,  
606 32, L11801, doi:10.1029/2004GL021821.  
607 Pan, L., J.C. Guille, D. P. Edwards, and P.L. Bailey (1998), Retrieval of tropospheric  
608 carbon monoxide for the MOPITT experiment, *J. Geophys. Res.*, 103, 32277-32290.  
609 Savtchenko A., R. Kummerer, P. Smith, A. Gopalan, S. Kempler, and G. (2008),  
610 Leptoukh, A-Train Data Depot: Bringing Atmospheric Measurements Together, *IEEE*  
611 *Trans. Geos. Rem. Sens.*, 46, No. 10, 2788-2795  
612 Seftor, C.J., N.C. Hsu, J.R. Herman, P.K. Bhartia, O. Torres, W.I. Rose, D.J. Schneider,  
613 and N. Krotkov (1997), Detection of volcanic ash clouds from Nimbus7/total ozone  
614 mapping spectrometer, *J. Geophys. Res.*, 102, 16,749-16,759  
615 Sinha, P., P. V. Hobbs, R. J. Yokelson, I. T. Bertschi, D. R. Blake, I. J. Simpson, S. Gao,  
616 T. W. Kirchstetter, and T. Novakov (2003), Emissions of trace gases and particles  
617 from savanna fires in southern Africa, *J. Geophys. Res.*, 108, 8487,  
618 doi:10.1029/2002JD002325.  
619 Susskind, J., C. D. Barnet, and J. M. Blaisdell (2003), Retrieval of atmospheric and  
620 surface parameters from AIRS/AMSU/HSB data in the presence of clouds, *IEEE*  
621 *Trans. Geosci. Remote Sens.*, 41, 390– 409.

622 Swap, R.J., H.J. Annegarn, J.T. Suttles, M.D. King, S. Platnick, J.L. Privette, and R.J.  
623 Scholes (2003), Africa Burning: A thematic analysis of the Southern African Regional  
624 Science Initiative (SAFARI 2000), *J. Geophys. Res.*, 108(D13), 8465,  
625 doi:10.1029/2003JD003747

626 Toledano, C., M. Wiegner, S. GROß, V. freudenthaler, J. Gasteiger, D. Muller, A.  
627 Schladitz, B. Weinzierl, B. Torres, and N.T. O'Neill (2011), Optical properties of  
628 aerosol mixtures from sun-sky radiometry during SAMUM-2, *Tellus* 63B, 635-648.

629 Torres O., P.K. Bhartia, J.R. Herman and Z. Ahmad (1998), Derivation of aerosol  
630 properties from satellite measurements of backscattered ultraviolet radiation.  
631 Theoretical Basis, *J. Geophys. Res.*, 103, 17099-17110

632 Torres, O., P.K. Bhartia, J.R. Herman, A. Syniuk, P. Ginoux, and B. Holben (2002), A  
633 long term record of aerosol optical depth from TOMS observations and comparison to  
634 AERONET measurements, *J. Atm. Sci.*, 59, 398-413

635 Torres, O., A. Tanskanen, B. Veihelman, C. Ahn, R. Braak, P. K. Bhartia, P. Veefkind,  
636 and P. Levelt (2007), Aerosols and surface UV products from OMI Observations: an  
637 overview, *J. Geophys. Res.*, 112, D24S47, doi:10.1029/2007JD008809

638 Turquety, S., Hurtmans, D., Hadji-Lazaro, J., Coheur, P.-F., Clerbaux, C., Josset, D., and  
639 Tsamalis, C. (2009), Tracking the emission and transport of pollution from wildfires  
640 using the IASI CO retrievals: analysis of the summer 2007 Greek fires, *Atmos. Chem.*  
641 *Phys.*, 9, 4897-4913, doi:10.5194/acp-9-4897-2009.

642 Winker, D. M., J. Pelon, and M. P. McCormick, 2003: "The CALIPSO mission:  
643 Spaceborne lidar for observation of aerosols and clouds", *Proc. SPIE*, 4893, pp. 1-11.  
644  
645  
646  
647  
648  
649  
650  
651  
652  
653  
654  
655  
656  
657  
658  
659  
660  
661  
662  
663  
664  
665  
666  
667

668 **Figure Captions**

669

670 **Figure 1.** Graphic description of OMAERUV inversion scheme.

671 **Figure 2.** OMAERUV Aerosol Index on July 7, 2006 (a), AIRS CO amounts (b)

672 (c) Aerosol type classification

673 **Figure 3.** Aerosol type over Africa on August 27, 2007 (see text for details)

674 **Figure 4.** CALIOP-measured attenuated backscatter profiles at 532 nm (solid line) at

675 1064 nm (dotted line) over Amazonia (left) and Saharan Desert (right).

676 **Figure 5.** Sample derived aerosol layer height and CALIOP-measured 1064 nm

677 backscatter for three aerosol episodes: top: top; middle, middle; bottom: bottom.

678 **Figure 6.** Monthly average aerosol layer height.

679 **Figure 7.** Evaluation of AOD retrieval using standard aerosol layer height assumption

680 (left) and CALIOP climatology (right) at the Banizoumbou site.

681 **Figure 8.** Retrieved AOD and SSA at 388 nm from the previous (a, b) and improved (c,

682 d) OMI UV algorithm over Northeastern China on Aug 20, 2007.

683

684

685

686

687

688

689

690

691

692

693

694

695

696

697

698

699

700 Table 1

AERONET Site	Location		Number points	R		Intercept		RMS		Q <sub>10</sub>		Q <sub>30</sub>	
	Lat.	Lon.		Std	Cal	Std.	Cal	Std.	Cal	Std	Cal	Std	Cal
Agoufou	15.3N	1.5E	184	0.82	0.83	0.13	0.10	0.17	0.16	50	58	64	71
Tamanrasset	22.8N	5.5E	98	0.83	0.84	0.09	0.08	0.10	0.10	60	63	66	69
Banizombou	13.5N	2.7E	182	0.71	0.75	0.21	0.17	0.19	0.16	45	53	57	67
Dakar	14.4N	17.0W	163	0.73	0.74	0.14	0.12	0.19	0.15	39	56	58	69
IER Cinzana	13.3N	5.9W	118	0.79	0.83	0.09	0.08	0.21	0.17	35	47	50	60

701

702

703

704

705

706

707

708

709

710

711

712

713

714

715

716

717

718

719

720

721

722

723

724

725

726

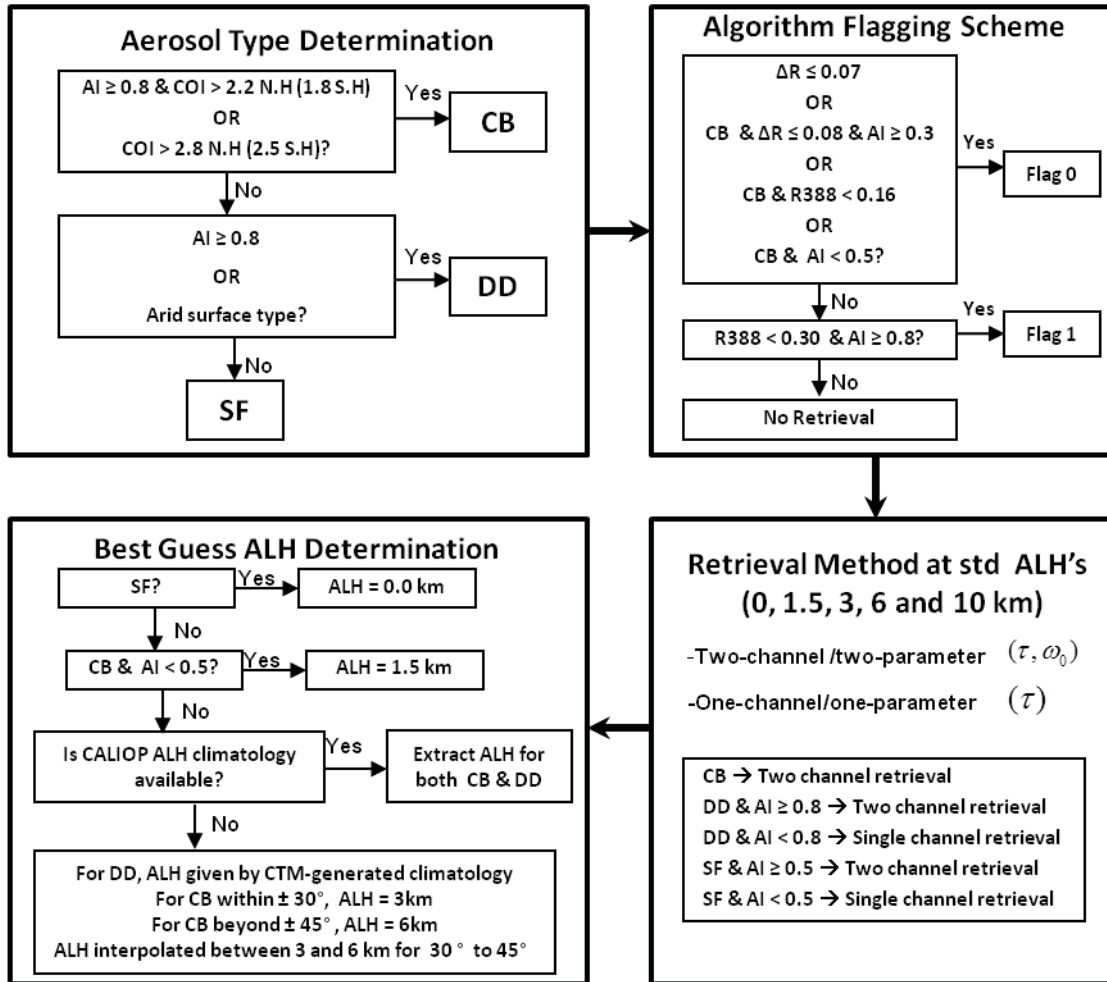
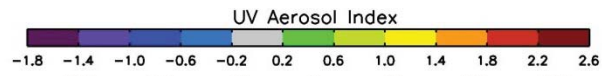
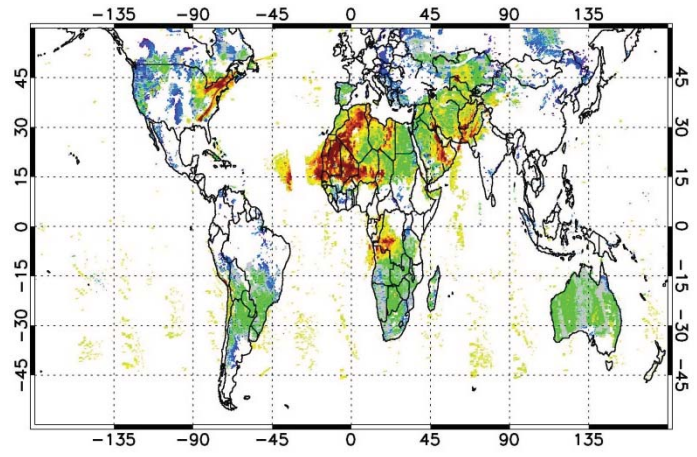


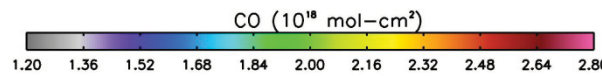
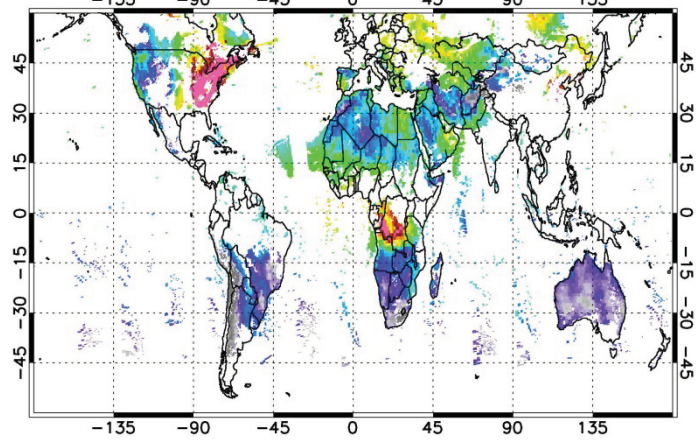
Figure 1

727  
728  
729  
730  
731  
732  
733  
734  
735  
736  
737  
738  
739  
740  
741  
742  
743  
744  
745  
746  
747

748



749



750

751

752

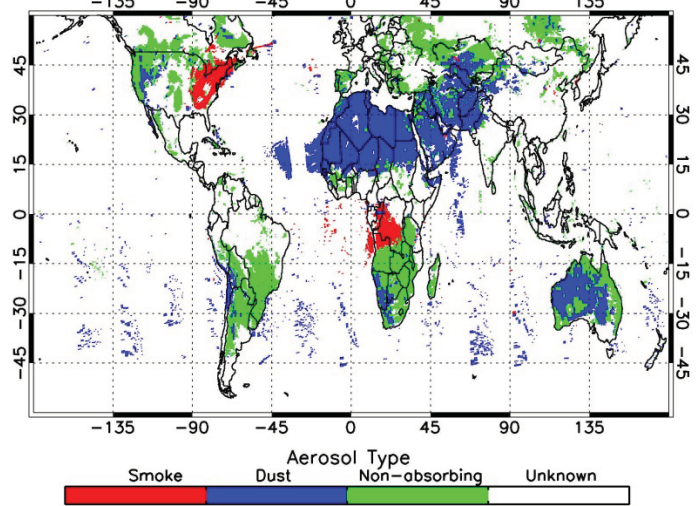


Figure 2

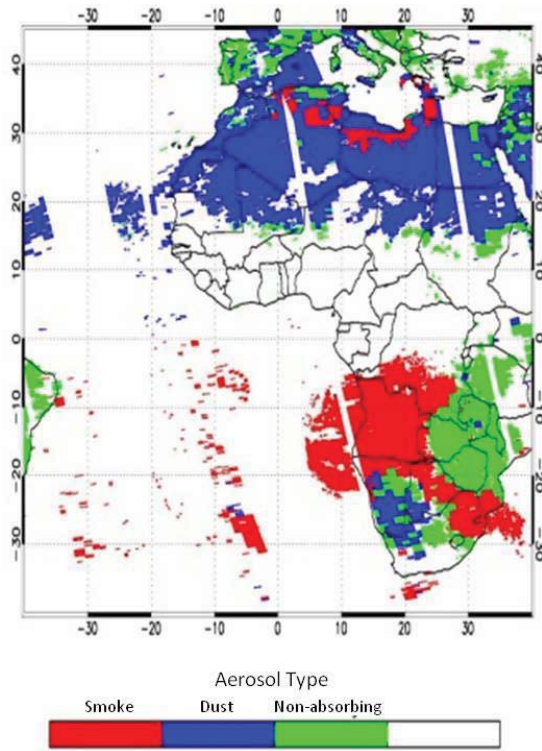


Figure 3

753  
754  
755  
756  
757  
758  
759  
760  
761  
762  
763  
764  
765  
766  
767  
768  
769  
770  
771



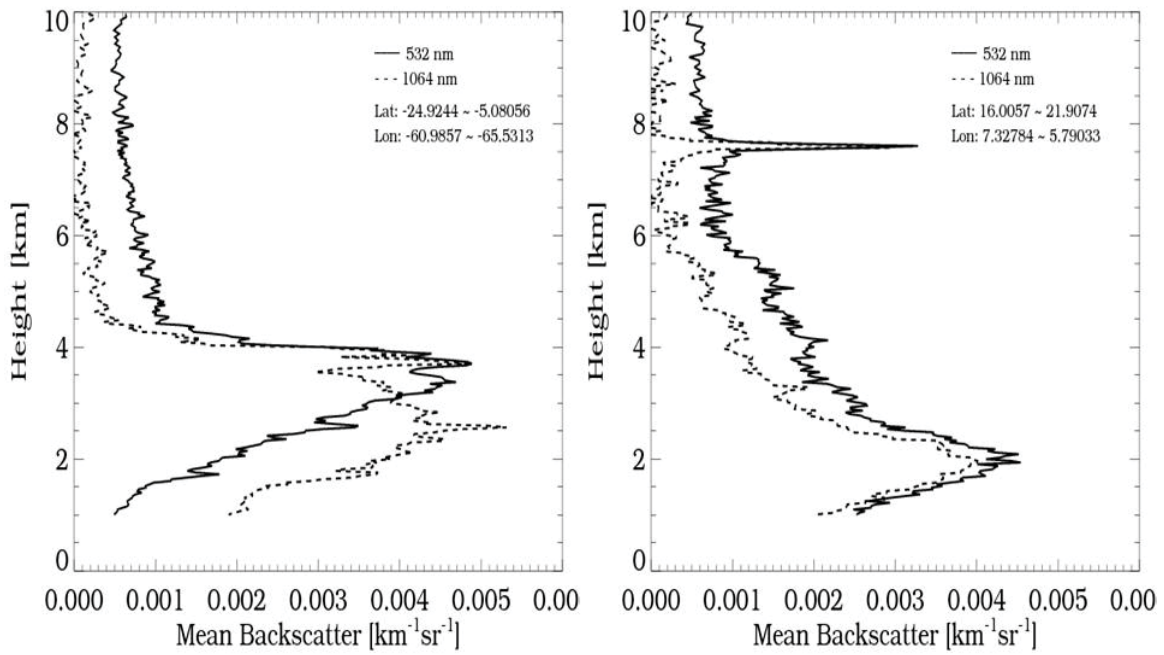
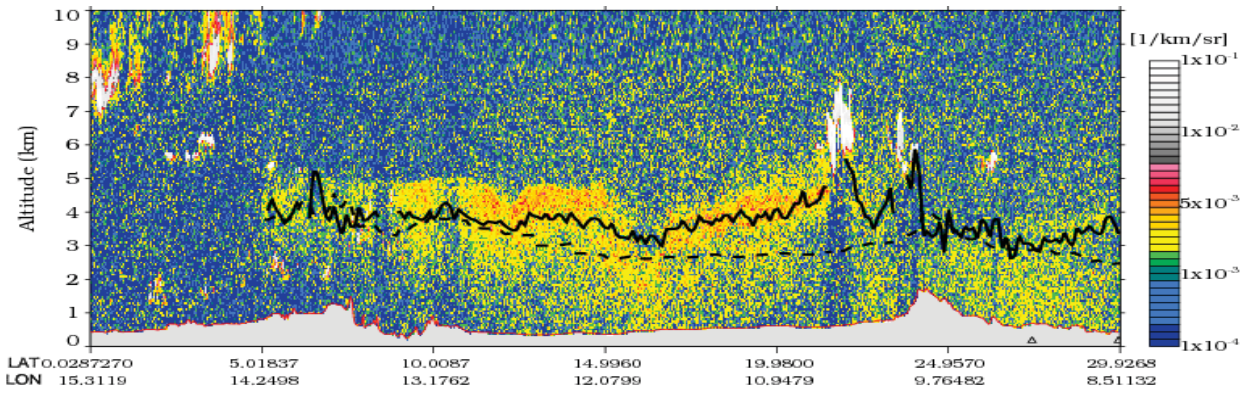


Figure 4.

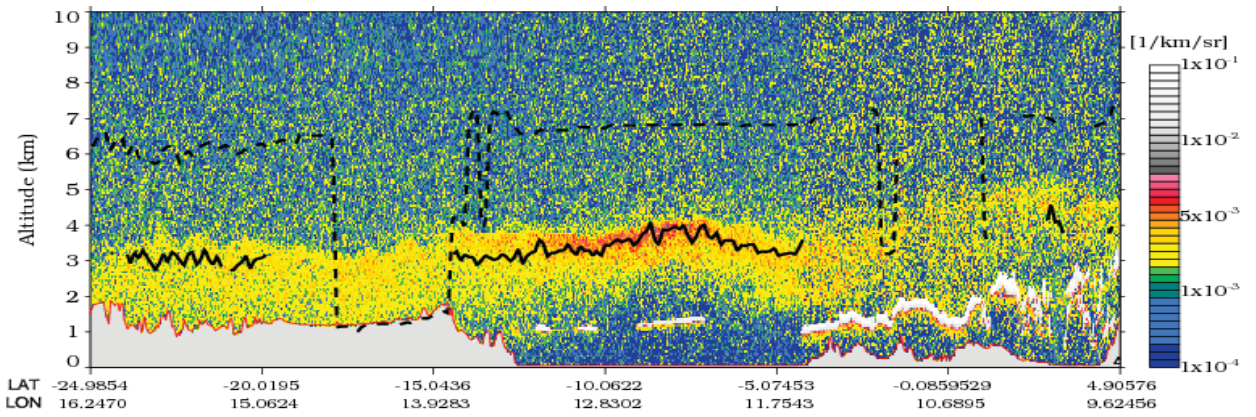
772  
 773  
 774  
 775  
 776  
 777  
 778  
 779  
 780  
 781  
 782  
 783  
 784  
 785  
 786  
 787  
 788  
 789  
 790



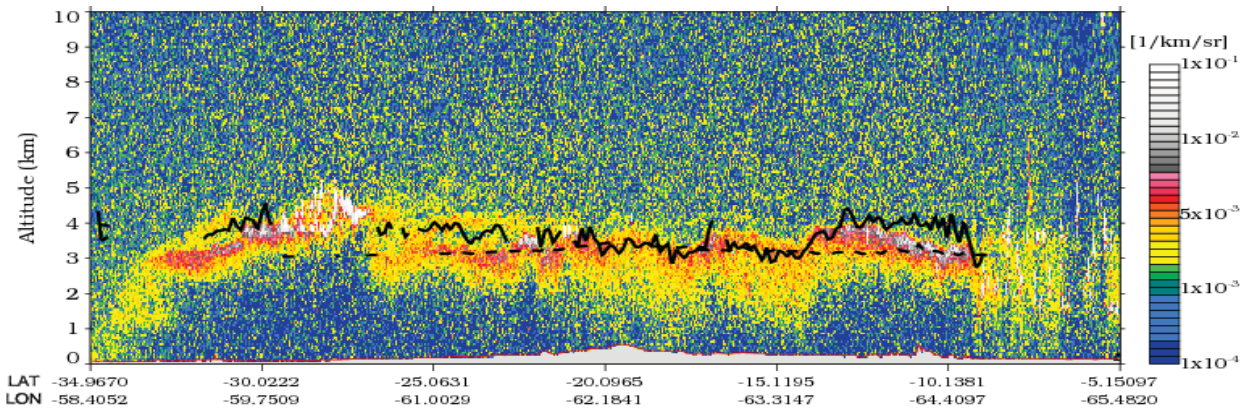
791



792



793



794

795 Figure 5.

796

797

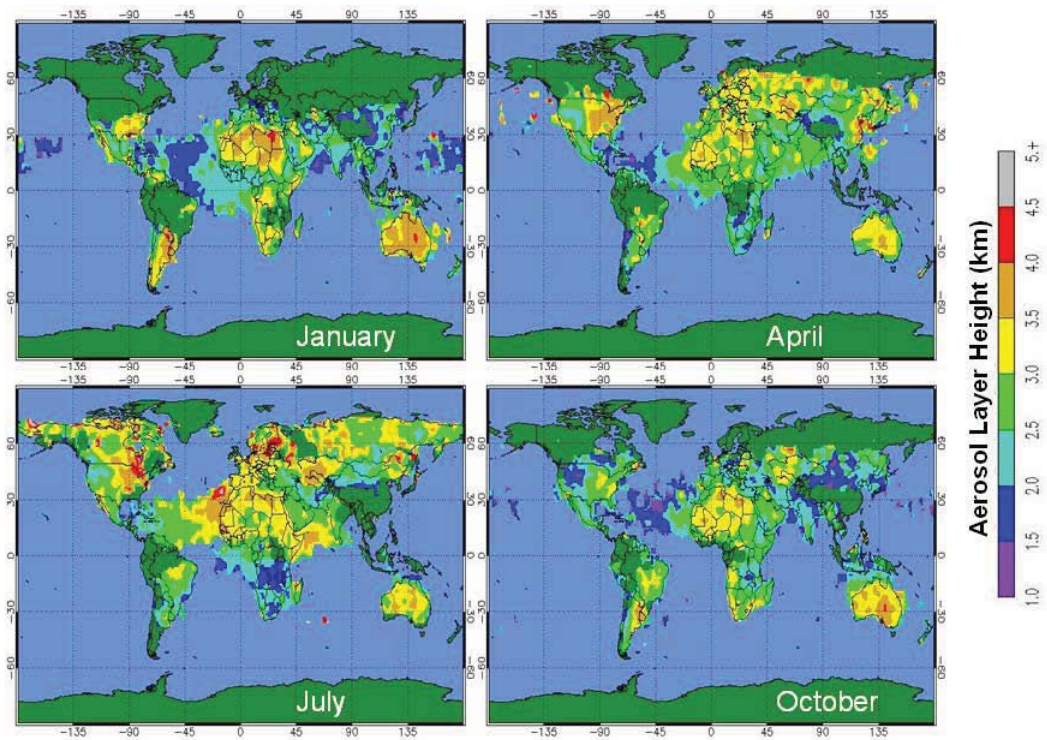
798

799

800

801

802



803

804 Figure 6

805

806

807

808

809

810

811

812

813

814

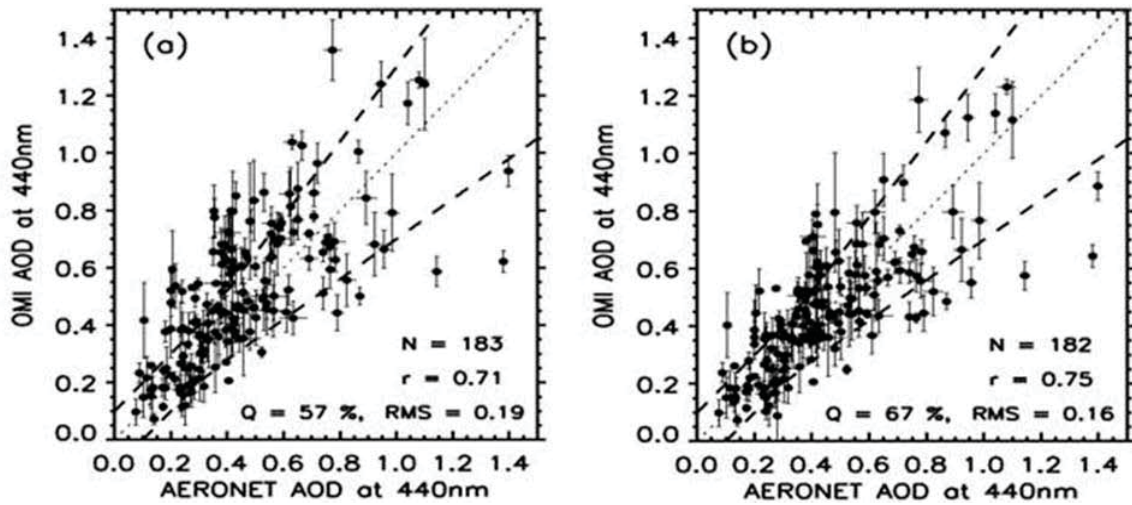
815

816

817

818

819



820

821 Figure 7

822

823

824

825

826

827

828

829

830

831

832

833

834

835

836

837

838

839

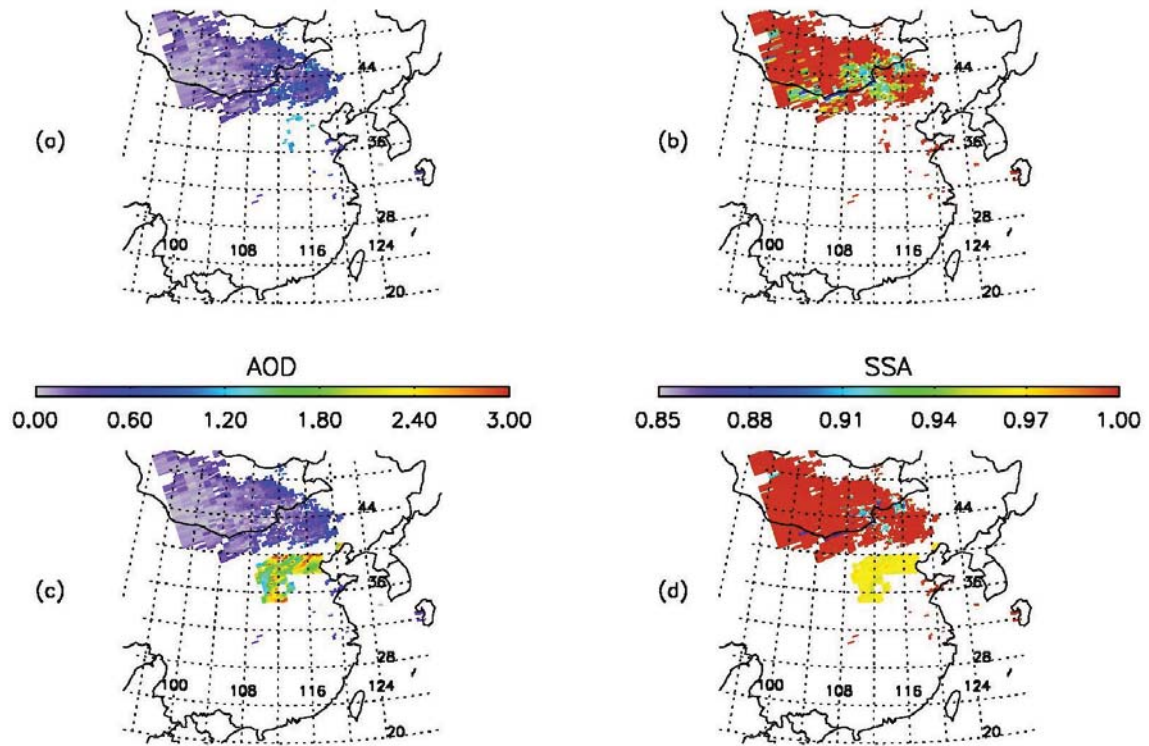
840

841

842



843



844

845 Figure 8.

846

847

848

849

850

851

852

853

854

855

856

857

858

859

860